Letter

Toroidal nonreciprocity of optical second harmonic generation

J. Mund [1], D. R. Yakovlev [1,2], A. N. Poddubny [2], R. M. Dubrovin [2], M. Bayer [1,2] and R. V. Pisarev [2,*]

[1] *Experimentelle Physik 2, Technische Universität Dortmund, D-44221 Dortmund, Germany*

[2] *Ioffe Institute, Russian Academy of Sciences, 194021 St. Petersburg, Russia*

(Received 8 September 2020; revised 10 March 2021; accepted 11 May 2021; published 28 May 2021)

We demonstrate mechanisms of reciprocity breaking in nonlinear optics driven by the toroidal dipole moment which characterizes nontrivial spatial distributions of spins in solids. Using high-resolution femtosecond spectroscopy at electronic resonances in the magnetoelectric antiferromagnet CuB_2O_4, we show that nonreciprocity reaches 100% for opposite magnetic fields due to the interference of nonlinear coherent sources of second harmonic generation originating from the toroidal dipole moment, applied magnetic field, and noncentrosymmetric crystal structure. The experimental results are corroborated by theoretical analysis based on the crystal and magnetic symmetry of CuB_2O_4. Our findings open degrees of freedom in nonlinear optics and pave the way for future nonreciprocal spin-optronic devices operating on the femtosecond timescale.

DOI: 10.1103/PhysRevB.103.L180410

The Lorentz reciprocity principle is a fundamental concept that governs light propagation in optically linear media in the absence of magnetic fields [1–3]. In nonlinear optics, the principle of reciprocity is not valid even in the absence of a magnetic field [4,5]. A bunch of nonlinear nonreciprocal effects can become especially diverse for the structures with broken spatial inversion symmetry and nontrivial spin order. Despite rapid recent progress, many novel light-matter coupling effects enabled by the interplay of nonlinearity, external magnetic fields, and nontrivial spin order can be still envisaged [6–9].

Here, we demonstrate experimentally widely tunable nonlinear nonreciprocity due to interference of symmetry-different optical second harmonic generation (SHG) sources induced by a toroidal dipole moment $\boldsymbol{T}$, an applied magnetic field $\boldsymbol{B}$, and noncentrosymmetric crystal structure. The toroidal dipole moment for a localized distribution of spins $\boldsymbol{S}_j$ can be written as $\boldsymbol{T} = \frac{1}{2}\sum_j \boldsymbol{r}_j \times \boldsymbol{S}_j$ and can be viewed as a magnetoelectric dipole moment in addition to the electric and magnetic dipoles [10]. It changes sign under both space inversion and time-reversal symmetry operations. The rigorous generalization of the toroidal dipole moment for infinite crystals was recently presented in Ref. [11]. Currently, the toroidal order is attracting tremendous attention across the disciplines ranging from high-energy physics [12], spin physics of multiferroics and magnetoelectrics [7,11,13–20] to nanoscale optics [21]. However, the role and manifestations of the toroidal moment in the SHG processes have never been reported, to the best of our knowledge.

For solving these tasks, we have chosen an antiferromagnet CuB_2O_4 which belongs to the promising class of magnetoelectric and multiferroic materials with potentially important practical applications [22–25]. This crystal possesses a favorable combination of noncentrosymmetric crystal structure [26], commensurate and incommensurate types of antiferromagnetic spin ordering [27,28]. In particular, it demonstrates exceptionally narrow optical resonances [29–31] which provide rich opportunities for the studies of symmetry-different contributions to the SHG processes. All these factors open up yet unexplored possibilities for disclosing new mechanisms of SHG nonreciprocity on the spectroscopic level but not only at a single wavelength when different mechanisms may overlap becoming indistinguishable. Here, we focus on the SHG at the 1.405 eV electronic resonance [Fig. 1(a)] at the crystal-field-split $3d^9$ states of the Cu^{2+} ions [29,30,32]. While SHG at this transition was observed before [29,32], neither the SHG nonreciprocity nor SHG fine structure and involved mechanisms have been studied or analyzed so far. We are confident that our experimental results provide a solid basis for revealing the complex nature of the SHG nonreciprocity at the microscopic level.

In this Letter we report on the SHG nonreciprocity due to the nonlinear coupling of coherent light with commensurate and incommensurate spin structures formed by spins $S = \frac{1}{2}$ of Cu^{2+} ions [27,28]. The nonvanishing antiferromagnetic $\boldsymbol{L}^{\pm} = \pm(\boldsymbol{S}_1 - \boldsymbol{S}_2)$ and ferromagnetic $\boldsymbol{M}^{\pm} = \pm(\boldsymbol{S}_1 + \boldsymbol{S}_2)$ order parameters characterize the two types of antiferromagnetic domains in the commensurate phase, respectively [27]. Crucially, the commensurate antiferromagnetic phase carries not only the order parameter $\boldsymbol{L}$ but also a nonzero toroidal dipole vector, described in detail in the Supplemental Material (SM) [33]. The behavior of the toroidal vector is dictated by the antiferromagnetic moment, $\boldsymbol{T} \propto L_x\hat{\boldsymbol{y}} + L_y\hat{\boldsymbol{x}}$. In the considered commensurate phase when $\boldsymbol{L}$ is along [110] $L_x = \pm L_y$, so $\boldsymbol{T} \parallel \boldsymbol{L}$. When the magnetic field is applied, the CuB_2O_4 possesses the time-noninvariant toroidal ($\boldsymbol{T} \parallel \boldsymbol{L}$) and magnetic-field-induced ($\boldsymbol{B}$) SHG sources which are also complemented by the time-invariant crystallographic (C) SHG source due to the noncentrosymmetric crystal structure. Under certain conditions, these sources can interfere constructively or destructively as shown schematically in Fig. 1(a). One can achieve full control of nonreciprocity by changing the direction and magnitude of the applied magnetic field. Obviously,

*pisarev@mail.ioffe.ru

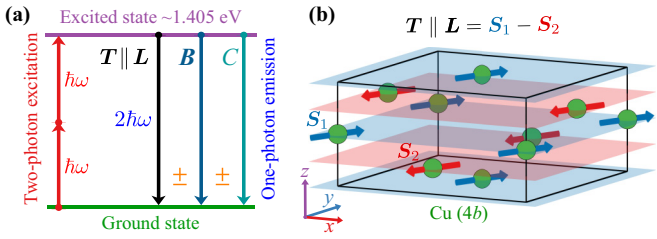

FIG. 1. (a) Coherent SHG processes at the optical transition within the Cu^{2+} ions near 1.405 eV between the ground and the lowest excited states when the two E^{ω} photons are converted into a single $E^{2\omega}$ photon. The vertical ($\boldsymbol{T} \parallel \boldsymbol{L}$), ($\boldsymbol{B}$), and ($C$) lines mark the SHG sources due to the toroidal, magnetic-field-induced, and crystallographic sources which can interfere constructively or destructively as indicated by the ± signs. (b) A crystallographic unit cell of tetragonal CuB_2O_4 with antiferromagnetic spins oriented along the [110] axis in the commensurate state. At equilibrium, the antiferromagnetic moment $\boldsymbol{L} = \boldsymbol{S}_1 - \boldsymbol{S}_2$ and the toroidal moment $\boldsymbol{T}$ are collinear and are also aligned along the [110] axis.

the interference of these and other SHG sources, for example those due to quadrupole and magnetic dipole sources allowed in centrosymmetric materials, is not limited to CuB_2O_4, but can be regarded as a new concept for magnetic routing of the nonlinear coherent emission in complex media.

For experimental detection of SHG processes and distinguishing different nonreciprocal contributions we used a spectroscopic technique based on wavelength tunable femtosecond laser with pulses at the 30 kHz repetition rate [40]. This technique provides high sensitivity and high spectral resolution, limited only by the spectrometer for dispersing the signals as described in Sec. S1 in the SM [33]. The method was applied to the (xz)-plane single-crystal CuB_2O_4 sample with the incident and SHG light propagating along the y axis, $\boldsymbol{k} \parallel y$. The crystallographic unit cell of tetragonal CuB_2O_4 with lattice parameters $a = b \neq c$ [26], where $a \parallel x$, $b \parallel y$, $z \parallel c$ is shown in Fig. 1(b). For more details about CuB_2O_4 crystal symmetry see Sec. S2 in the SM [33]. The covered temperature range 1.9–25 K includes several phase transitions between commensurate and incommensurate antiferromagnetic spin structures, as well as the antiferromagnetic–paramagnetic phase transition at $T_N =$ 20 K [28]. The magnetic field B up to ±10 T was applied along the x and z crystal axes in the two Voigt geometries, $\boldsymbol{k} \perp \boldsymbol{B}$, that allowed us to test the symmetry-different manifestations of SHG toroidal nonreciprocity related to notably different magnetic phase diagrams [28,33]. SHG rotational anisotropies were measured for the crossed $\boldsymbol{E}^{\omega} \perp \boldsymbol{E}^{2\omega}$ and parallel $\boldsymbol{E}^{\omega} \parallel \boldsymbol{E}^{2\omega}$ light polarizations as a function of the $\boldsymbol{E}^{\omega}$ polarization angle. Experimental rotational anisotropies were fitted using appropriate equations derived on the basis of the crystallographic and magnetic symmetry of CuB_2O_4 that allowed us to distinguish symmetry-different contributions to the SHG (see Sec. S3 in the SM [33]).

Figure 2(a) shows the SHG spectra at $T = 4.0$ K in opposite magnetic fields ±8 T applied along the x axis when the antiferromagnetic structure is commensurate. The highest SHG intensity is observed at the 1.4047 eV line in the $\boldsymbol{E}^{\omega} \perp \boldsymbol{E}^{2\omega}$ polarization configuration and for the azimuthal angle $\phi = 0^{\circ}$ corresponding to $\boldsymbol{E}^{2\omega} \parallel \boldsymbol{B} \parallel x$. The spectra are divided into the two Frenkel groups of sharp lines at 1.4047–1.4049 eV (G1) and 1.4062–1.4063 eV (G2) with full widths at half maximum (FWHM) below 100 μeV. Observation of small splittings on the order of 0.5 meV within each group demonstrates the advantages of the femtosecond-pulse technique providing high spectral resolution. Previous studies of SHG in CuB_2O_4 with the use of the nanosecond-pulse technique did not resolve the two Frenkel components [29]. Additionally, the G1 and G2 groups are separated by the Zeeman splitting of about 1.5 meV at $B_x = 8$ T. The main result shown in Fig. 2(a) is the strong difference between the SHG spectra for opposite ±8 T magnetic fields marked by black and red symbols and lines. That is an unequivocal proof

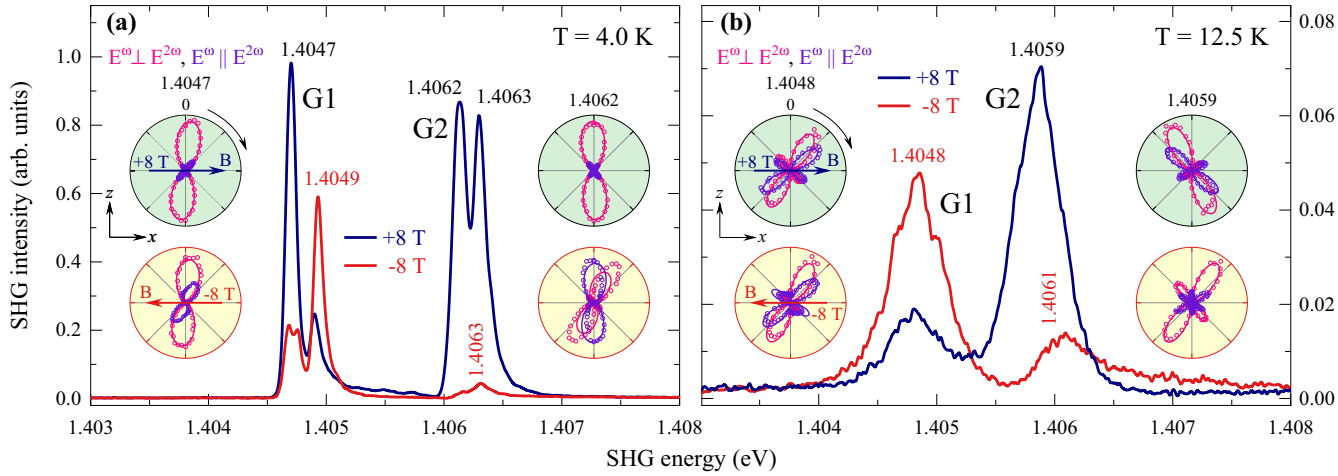

FIG. 2. Nonreciprocal SHG spectra of CuB_2O_4 (xz-plane sample) at (a) $T = 4.0$ K and (b) $T = 12.5$ K measured at normal incidence $\boldsymbol{k} \parallel y$, $\boldsymbol{E}^{\omega} \parallel z$, $\boldsymbol{E}^{\omega} \perp \boldsymbol{E}^{2\omega}$, $\boldsymbol{B} = \pm 8$ T $\parallel x$. SHG spectra at $T = 4.0$ K for opposite fields demonstrate strong spectrally varying nonreciprocity achieving almost 100% for some lines, e.g., for the 1.4062 eV line. When the temperature is increased from $T = 4.0$ to 12.5 K, the SHG intensity decreases by about an order of magnitude but the nonreciprocity remains well pronounced. Blue and yellow insets show rotational anisotropy diagrams for the two G1 and G2 SHG groups for opposite magnetic fields, respectively.

of giant SHG nonreciprocity whose degree varies for different lines and approaches 100% at some photon energies, e.g., for the 1.4062 eV line. As the temperature is raised up to 12.5 K [Fig. 2(b)], the SHG lines broaden, but the splitting into two groups and the nonreciprocity remain well pronounced.

The SHG nonreciprocity is further confirmed by the rotational anisotropy diagrams [see insets to Figs. 2(a) and 2(b)] for the two polarization configurations $\boldsymbol{E}^{\omega} \perp \boldsymbol{E}^{2\omega}$ (magenta symbols) and $\boldsymbol{E}^{\omega} \parallel \boldsymbol{E}^{2\omega}$ (blue symbols). We note that the diagrams for opposite fields at $T = 4.0$ and 12.5 K are similar for the G1 group of lines but very different for the G2 group. All these particular features of diagrams give us an opportunity to analyze contributions to SHG as discussed in Sec. S3 in the SM [33].

The crystallographic SHG vanishes at normal incidence and we explain the observed SHG nonreciprocity in the $\boldsymbol{B} \parallel x$ geometry by taking into account the interference of the two SHG sources due to the applied magnetic field, $E_x^{2\omega} \propto (E_z^{\omega})^2 B_x$ and the toroidal moment $\boldsymbol{T}$, $\boldsymbol{E}^{2\omega} \propto (E_z^{\omega})^2 \boldsymbol{T}$. The interference results in nonreciprocal SHG as

$$|E^{2\omega}(\boldsymbol{B})|^2 - |E^{2\omega}(-\boldsymbol{B})|^2 \propto B_x T_x \left|E_z^{\omega}\right|^4. \qquad (1)$$

We note that this equation is valid only in the commensurate magnetic phase because in the incommensurate phase the toroidal moment vanishes. The toroidal moment $\boldsymbol{T}$ in CuB_2O_4 in zero field is aligned with the [110] axis [27,33]. More formally, in the given geometry the observed SHG is due to the nonlinear magnetoelectric susceptibility $C^L_{xzzy} = C^L_{yzzx}$, and nonlinear magnetic-field-induced susceptibility $C^B_{xzzx} = -C^B_{yzzy}$ tensor components introduced in Sec. S2 in the SM [33].

Detailed analysis of rotational anisotropies in Figs. 2(a) and 2(b) shows that Eq. (1) being derived only in the electric-dipole approximation is not sufficient to obtain unambiguous fittings and indicates the presence of other nonreciprocity mechanisms. In fact, the noncentrosymmetric crystal structure of CuB_2O_4 allows for both electric-dipole and magnetic-dipole SHG contributions. For fitting data in insets in Figs. 2(a) and 2(b) we used Eq. (S18) and numerical results are listed in Table III in the SM [33]. The rotational anisotropies at $T = 4.0$ K are mostly governed by the electric dipole terms as expressed by Eq. (1). This is solid evidence of the dominant magnetotoroidal electric dipole SHG nonreciprocity at this temperature. However, the data at $T = 12.5$ K clearly indicate a notable magnetic dipole contribution to the SHG, which leads to the azimuthal rotation of anisotropy diagrams around the y axis in the insets to Fig. 2(b). It is clockwise for G1 and counterclockwise for G2 lines. Evidently, a microscopic theory is required for explaining these important and interesting results, but this task is beyond the scope of our Letter.

According to the magnetic phase diagrams discussed in several publications [27,28,32], the orientation of the $\boldsymbol{T} \parallel \boldsymbol{L}$ vectors is sensitive to the direction and magnitude of the applied magnetic field in the (xy) plane. Indeed, while at zero field these vectors are directed along the easy [110] axis, when the B_x field is increased, they gradually rotate toward the y axis overcoming the magnetic anisotropy and resulting in modification of the SHG response.

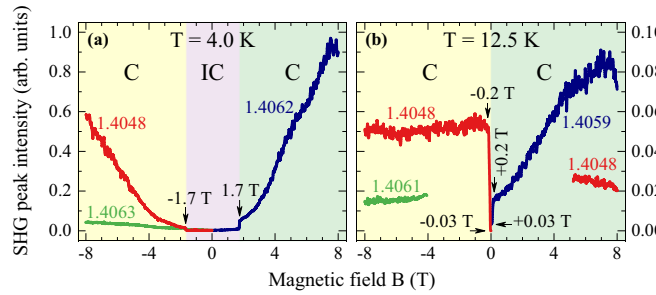

FIG. 3. Magnetic field dependencies ($\boldsymbol{B} \parallel x$) of the SHG at (a) $T = 4.0$ K and (b) $T = 12.5$ K. Purple and yellow/blue regions correspond to incommensurate (IC) and commensurate (C) magnetic phases shown schematically on the basis of Refs. [28,38]. The numbers on the lines indicate energy of the SHG lines. Note the scale difference by an order of magnitude in panels (a) and (b).

An important result is shown in Fig. 3(a) where no SHG signals are detected in the incommensurate phase (purple region) where the toroidal moment vanishes but are readily observable in the commensurate phases (yellow and blue regions). According to the neutron diffraction studies [27], the incommensurate antiferromagnetic structure of CuB_2O_4 can be described as the rotation of the $\boldsymbol{L}$ vector in the (xy) plane, while propagating along the z axis when the orientation distribution of $\boldsymbol{T} \parallel \boldsymbol{L}$ vectors is not defined. As a consequence of such spin distribution, the SHG signals disappear. The SHG signal jumps from zero to finite values only when the phase boundary between the incommensurate and commensurate phases is crossed [Fig. 3(a)] and then it changes strongly with growing magnetic field.

Field dependencies of SHG at $T = 4.0$ K [Fig. 3(a)] and 12.5 K in the commensurate phase [Fig. 3(b)] are drastically different. The SHG intensity is decreased by about a factor of 10 (compare the intensity scales in both figures). In the incommensurate phase the SHG signal is fully suppressed, but it is readily observed in the commensurate phase in fields larger than ± 0.03 T. We suppose that these field values correspond to the disappearance of antiferromagnetic domains. The SHG field dependencies are strongly nonreciprocal and each line demonstrates specific behavior. Pronounced temperature changes of the rotational anisotropies are observed when comparing the insets in Figs. 2(a) and 2(b). These intriguing effects require a detailed microscopic analysis which is beyond the scope of our Letter.

Figure 4(a) shows the SHG results at $T = 12.5$ K for the opposite magnetic fields $B = \pm 5$ T applied along the tetragonal z axis, $\boldsymbol{B} \parallel z$, and the results are radically different from those for the $\boldsymbol{B} \parallel x$ geometry of Fig. 2(b). In both these cases CuB_2O_4 is in the commensurate phase and the spectra are composed of the two G1 and G2 Frenkel groups. The strongest SHG signals are observed for the $\boldsymbol{E}^{\omega} \parallel z$ and $\boldsymbol{E}^{2\omega} \parallel x$ orthogonal polarizations, respectively. However, in striking contrast to the $\boldsymbol{B} \parallel x$ geometry where the SHG nonreciprocity reaches values as high as 100% for opposite field directions, in the $\boldsymbol{B} \parallel z$ geometry the SHG spectra are exactly identical for opposite fields and no nonreciprocity is detected. Since the crystallographic SHG contribution [C type in Fig. 1(a)] vanishes at normal incidence, $\boldsymbol{k} \parallel y$, the

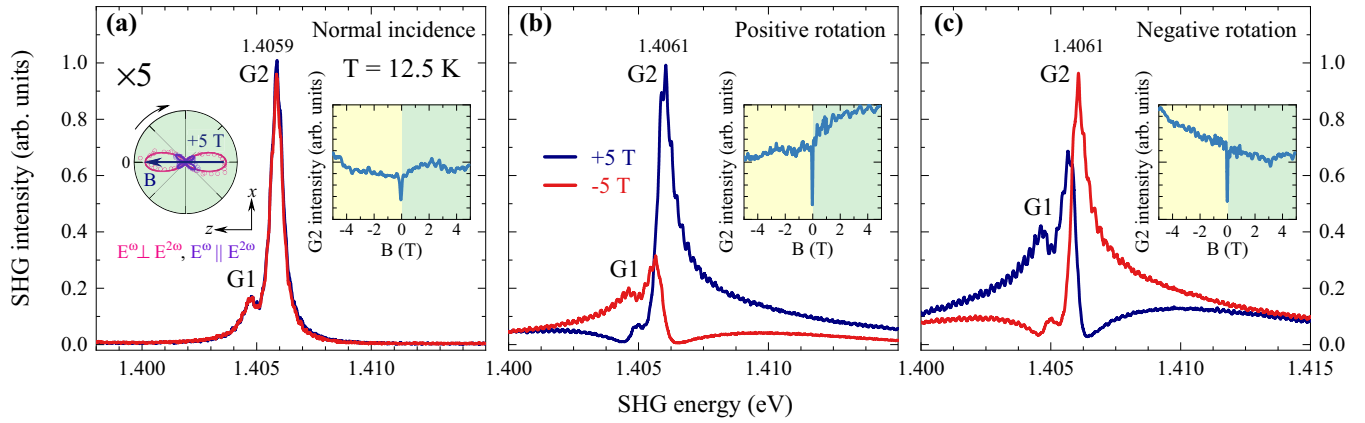

FIG. 4. SHG spectra of CuB_2O_4 at (a) normal incidence $\boldsymbol{k} \parallel y$ in the Voigt geometry, $\boldsymbol{E}^{\omega} \parallel z$, $\boldsymbol{E}^{\omega} \perp \boldsymbol{E}^{2\omega}$, $\boldsymbol{B} = \pm 5$ T $\parallel z$ and for the sample rotated by 5° in (b) positive and (c) negative directions around the x axis. The left inset to (a) shows SHG rotational anisotropy of the G2 peak for $\boldsymbol{E}^{\omega} \perp \boldsymbol{E}^{2\omega}$ (magenta symbols) and $\boldsymbol{E}^{\omega} \parallel \boldsymbol{E}^{2\omega}$ (blue symbols) and these anisotropies are similar for (b) and (c). Magnetic field SHG dependencies for the G2 peak shown in the right insets in (a), (b), and (c) figures are radically different in all three cases.

observed SHG spectra in Fig. 4(a) should be assigned to the antiferromagnetic/toroidal order parameter $\boldsymbol{L} \parallel \boldsymbol{T}$. In particular, at normal incidence [Fig. 4(a)], $\boldsymbol{k} \parallel y$, $\boldsymbol{B} \parallel z$, $\boldsymbol{E}^{\omega} \parallel z$, and $\boldsymbol{E}^{2\omega} \parallel x$, the SHG signal is induced by the only contribution $P_x^{2\omega} = C^L_{xzzy} E_z^{\omega} E_z^{\omega} L_y \propto C^L_{xzzy} E_z^{\omega} E_z^{\omega} T_x$ where C_{ijkl} are the relevant tensor components for nonlinear susceptibilities (see Sec. S2 in the SM [33]). Thus, no interference and no nonreciprocity are allowed since the detected SHG intensity $I^{2\omega} \propto (P_x^{2\omega})^2$ while the other SHG contributions are symmetry forbidden. In contrast to the well-pronounced field dependencies in Fig. 3(b), no field dependence is observed above the saturation field, as the right inset to Fig. 4(a) shows.

Following the fundamental rule that symmetry breaking can reveal new effects, we conducted experiments not only at normal incidence discussed above when magnetic-field-induced and crystallographic SHG contributions are symmetry forbidden, but also at oblique incidence when these contributions become allowed. The (xz) sample was rotated around the x axis by an angle of $\pm 5°$ while keeping unchanged the magnetic field and the incident/SHG light propagation directions, $\boldsymbol{B} \perp \boldsymbol{k}$. Under such rotations, the collinear incident/SHG wave vectors $\boldsymbol{k}$ do not exactly coincide with any of the x, y, or z axes. As a result, the SHG emission changes dramatically but in a different way for positive and negative sample rotation, as demonstrated in Figs. 4(b) and 4(c), respectively. A strong increase of the SHG intensity by about a factor of 5 is clear evidence of activation of the crystallographic SHG.

Namely, at oblique incidence both $E_y^{\omega} \neq 0$ and $E_z^{\omega} \neq 0$ and therefore the crystallographic polarization $P_x^{2\omega} = C_{xyz} E_y^{\omega} E_z^{\omega}$ becomes nonzero. The strongly asymmetric SHG spectra for positive and negative sample rotations [see Figs. 4(b) and 4(c)] immediately remind one of the Fano-type resonance [41–43]. It arises from the interference of the spectrally broad crystallographic SHG with the narrow resonant antiferromagnetic/toroidal SHG $P_x^{2\omega} = C^L_{xzzy} E_z^{\omega} E_z^{\omega} L_y$. Remarkably, the Fano asymmetry is inverted not only with the opposite sample rotations, but also for opposite magnetic fields thus evidencing the magnetic nonreciprocity. Since multiple magnetic-field-induced SHG sources become activated at the oblique incidence, it is challenging to pinpoint a specific single symmetry-allowed term responsible for the nonreciprocity observed in Figs. 4(b) and 4(c). One of such terms could be of the magnetic-dipole type $P_x^{2\omega} \propto k_y E_z^{\omega} E_z^{\omega} B_y$ that was discussed above when analyzing rotational anisotropies in insets to Figs. 2(a) and 2(b). This contribution becomes nonzero when the sample is tilted due to $B_y \neq 0$. Its sign changes for opposite magnetic fields resulting in SHG nonreciprocity.

It was a challenging task to make sure whether the SHG nonreciprocity survives when the $\boldsymbol{T} \parallel \boldsymbol{L}$ source vanishes above $T_N = 20$ K. In fact, experiments showed that nonreciprocity in opposite fields $B = \pm 10$ T can be reliably detected both at the normal incidence solely due to the applied field, as well as in the tilted samples due to interference of crystallographic and magnetic field sources (see Sec. S4 in the SM [33]).

In conclusion, we have demonstrated resonant SHG nonreciprocity in magnetoelectric antiferromagnet CuB_2O_4 using high-resolution femtosecond spectroscopic technique. The entirety of the results on spectral, magnetic field, temperature, and rotational anisotropy studies provided unambiguous evidences of nonreciprocity mechanisms related to the toroidal dipole moment which interfere with the applied magnetic field and crystallographic SHG sources. The SHG nonreciprocity was readily observed in the commensurate antiferromagnetic phases where the toroidal order parameter is strictly defined. In contrast, no SHG signal was observed in the incommensurate antiferromagnetic phases in which the toroidal order is destroyed. Analysis of the rotational anisotropy of SHG reveals both electric- and magnetic-dipole contributions, with the electric-dipole contribution being dominant at lower temperatures. Owing to the abilities of the femtosecond technique to observe fine structure of electronic transitions, our studies showed that CuB_2O_4 is a very fruitful platform for exploring various mechanisms of resonant and nonresonant nonlinear nonreciprocity. Obviously, such approach can be generalized to many other magnetic materials. Nonreciprocal effects, both

linear and nonlinear, are not only efficient tools for studies of electronic and magnetic structures of materials but are very promising for constructing novel nonreciprocal optical and microwave devices. In particular, these effects open up possibilities for the emerging field of antiferromagnetic spintronics and spin optronics [44–47].

Note added. Recently, we became aware of a paper on a similar study by S. Toyoda *et al.* [48]. We note that the results reported in this study have been obtained under notably different experimental conditions such as temperature and magnetic field range, as well as with different spectral resolution.

ACKNOWLEDGMENTS

We are grateful to M. A. Gorlach, E. L. Ivchenko, and M. Mostovoy for useful discussions. The samples used in our study were prepared from single crystals grown by L. N. Bezmaternykh. We acknowledge financial support by the Deutsche Forschungsgemeinschaft through the International Collaborative Research Centre 160 (project C8). A.N.P. acknowledges partial financial support by RFBR Project No. 19-52-12038-NNIO_a. R.M.D. and R.V.P. acknowledge financial support by RFBR Project No. 19-52-12063.

[1] R. J. Potton, Reciprocity in optics, Rep. Prog. Phys. **67**, 717 (2004).

[2] C. Caloz, A. Alù, S. Tretyakov, D. Sounas, K. Achouri, and Z.-L. Deck-Léger, Electromagnetic Nonreciprocity, Phys. Rev. Appl. **10**, 047001 (2018).

[3] A. K. Zvezdin and V. A. Kotov, *Modern Magnetooptics and Magnetooptical Materials* (Institute of Physics Publishing, Bristol/Philadelphia, 1997).

[4] Y. Shen, *The Principles of Nonlinear Optics* (Wiley, Hoboken, 2002).

[5] R. W. Boyd, *Nonlinear Optics* (Academic, New York, 2008).

[6] M. Fiebig, V. V. Pavlov, and R. V. Pisarev, Second-harmonic generation as a tool for studying electronic and magnetic structures of crystals, J. Opt. Soc. Am. B **22**, 96 (2005).

[7] Y. Tokura and N. Nagaosa, Nonreciprocal responses from non-centrosymmetric quantum materials, Nat. Commun. **9**, 3740 (2018).

[8] S.-W. Cheong, D. Talbayev, V. Kiryukhin, and A. Saxena, Broken symmetries, non-reciprocity, and multiferroicity, npj Quantum Mater. **3**, 19 (2018).

[9] S.-W. Cheong, SOS: Symmetry-operational similarity, npj Quantum Mater. **4**, 53 (2019).

[10] Y. I. Sirotin and M. P. Shaskolskaya, *Fundamentals of Crystal Physics* (MIR, Moscow, 1983).

[11] M.-T. Suzuki, T. Nomoto, R. Arita, Y. Yanagi, S. Hayami, and H. Kusunose, Multipole expansion for magnetic structures: A generation scheme for a symmetry-adapted orthonormal basis set in the crystallographic point group, Phys. Rev. B **99**, 174407 (2019).

[12] V. M. Dubovik and V. V. Tugushev, Toroid moments in electrodynamics and solid-state physics, Phys. Rep. **187**, 145 (1990).

[13] N. A. Spaldin, M. Fiebig, and M. Mostovoy, The toroidal moment in condensed-matter physics and its relation to the magnetoelectric effect, J. Phys.: Condens. Matter **20**, 434203 (2008).

[14] S. Toyoda, N. Abe, and T. Arima, Nonreciprocal Refraction of Light in a Magnetoelectric Material, Phys. Rev. Lett. **123**, 077401 (2019).

[15] J. Lehmann, C. Donnelly, P. M. Derlet, L. J. Heyderman, and M. Fiebig, Poling of an artificial magneto-toroidal crystal, Nat. Nanotechnol. **14**, 141 (2019).

[16] B. B. Van Aken, J.-P. Rivera, H. Schmid, and M. Fiebig, Observation of ferrotoroidic domains, Nature (London) **449**, 702 (2007).

[17] C. Ederer and N. A. Spaldin, Towards a microscopic theory of toroidal moments in bulk periodic crystals, Phys. Rev. B **76**, 214404 (2007).

[18] A. S. Zimmermann, D. Meier, and M. Fiebig, Ferroic nature of magnetic toroidal order, Nat. Commun. **5**, 4796 (2014).

[19] P. Tolédano, M. Ackermann, L. Bohatý, P. Becker, T. Lorenz, N. Leo, and M. Fiebig, Primary ferrotoroidicity in antiferromagnets, Phys. Rev. B **92**, 094431 (2015).

[20] P. Toledano, D. D. Khalyavin, and L. C. Chapon, Spontaneous toroidal moment and field-induced magnetotoroidic effects in $Ba_2CoGe_2O_7$, Phys. Rev. B **84**, 094421 (2011).

[21] A. E. Miroshnichenko, A. B. Evlyukhin, Y. F. Yu, R. M. Bakker, A. Chipouline, A. I. Kuznetsov, B. Luk'yanchuk, B. N. Chichkov, and Y. S. Kivshar, Nonradiating anapole modes in dielectric nanoparticles, Nat. Commun. **6**, 8069 (2015).

[22] M. Fiebig, Revival of the magnetoelectric effect, J. Phys. D: Appl. Phys. **38**, R123 (2005).

[23] W. Eerenstein, N. Mathur, and J. F. Scott, Multiferroic and magnetoelectric materials, Nature (London) **442**, 759 (2006).

[24] M. Fiebig, T. Lottermoser, D. Meier, and M. Trassin, The evolution of multiferroics, Nat. Rev. Mater. **1**, 16046 (2016).

[25] N. A. Spaldin and R. Ramesh, Advances in magnetoelectric multiferroics, Nat. Mater. **18**, 203 (2019).

[26] M. Martinez-Ripoll, S. Martinez-Carrera, and S. Garcia-Blanco, The crystal structure of copper metaborate, CuB_2O_4, Acta Crystallogr., Sect. B: Struct. Sci., Cryst. Eng. Mater. **27**, 677 (1971).

[27] M. Boehm, B. Roessli, J. Schefer, A. Wills, B. Ouladdiaf, E. Lelievre-Berna, U. Staub, and G. A. Petrakovskii, Complex magnetic ground state of CuB_2O_4, Phys. Rev. B **68**, 024405 (2003).

[28] A. E. Petrova and A. I. Pankrats, Copper metaborate CuB_2O_4 phase diagrams based on the results of measuring the magnetic moment, J. Exp. Theor. Phys. **126**, 506 (2018).

[29] R. V. Pisarev, I. Sänger, G. A. Petrakovskii, and M. Fiebig, Magnetic-Field Induced Second Harmonic Generation in CuB_2O_4, Phys. Rev. Lett. **93**, 037204 (2004).

[30] R. V. Pisarev, A. M. Kalashnikova, O. Schöps, and L. N. Bezmaternykh, Electronic transitions and genuine crystal-field parameters in copper metaborate CuB_2O_4, Phys. Rev. B **84**, 075160 (2011).

[31] K. N. Boldyrev, R. V. Pisarev, L. N. Bezmaternykh, and M. N. Popova, Antiferromagnetic Dichroism in a Complex Multisublattice Magnetoelectric CuB_2O_4, Phys. Rev. Lett. **114**, 247210 (2015).

[32] M. Fiebig, I. Sänger, and R. V. Pisarev, Magnetic phase diagram of CuB_2O_4, J. Appl. Phys. **93**, 6960 (2003).

[33] See Supplemental Material at http://link.aps.org/supplemental/10.1103/PhysRevB.103.L180410 for details on the experimental setup, symmetry analysis for the second harmonic generation, and additional experimental data, which contains Refs. [7,11,13,14,26–29,32,34–39].

[34] M. I. Aroyo, J. M. Perez-Mato, D. Orobengoa, E. Tasci, G. de la Flor, and A. Kirov, Crystallography online: Bilbao crystallographic server, Bulg. Chem. Commun. **43**, 183 (2011).

[35] M. S. Dresselhaus, G. Dresselhaus, and A. Jorio, *Group Theory. Application to the Physics of Condensed Matter* (Springer-Verlag, Berlin/Heidelberg, 2008).

[36] S. N. Martynov and A. D. Balaev, Frustration mechanism of formation of a helical magnetic structure in the CuB_2O_4 two-subsystem antiferromagnet, JETP Lett. **85**, 649 (2007).

[37] Y. Kousaka, S. Yano, J. Kishine, Y. Yoshida, K. Inoue, K. Kikuchi, and J. Akimitsu, Chiral magnetic ordering and commensurate-to-incommensurate transition in CuB_2O_4, J. Phys. Soc. Jpn. **76**, 123709 (2007).

[38] T. Kawamata, N. Sugawara, S. M. Haidar, T. Adachi, T. Noji, K. Kudo, N. Kobayashi, Y. Fujii, H. Kikuchi, M. Chiba *et al.*, Thermal conductivity and magnetic phase diagram of CuB_2O_4, J. Phys. Soc. Jpn. **88**, 114708 (2019).

[39] I. E. Dzyaloshinskii, On the magneto-electrical effect in antiferromagnets, Sov. Phys. JETP **37**, 881 (1959).

[40] J. Mund, D. Fröhlich, D. R. Yakovlev, and M. Bayer, High-resolution second harmonic generation spectroscopy with femtosecond laser pulses on excitons in Cu_2O, Phys. Rev. B **98**, 085203 (2018).

[41] U. Fano, Effects of configuration interaction on intensities and phase shifts, Phys. Rev. **124**, 1866 (1961).

[42] A. E. Miroshnichenko, S. Flach, and Y. S. Kivshar, Fano resonances in nanoscale structures, Rev. Mod. Phys. **82**, 2257 (2010).

[43] M. F. Limonov, M. V. Rybin, A. N. Poddubny, and Y. S. Kivshar, Fano resonances in photonics, Nat. Photonics **11**, 543 (2017).

[44] V. Baltz, A. Manchon, M. Tsoi, T. Moriyama, T. Ono, and Y. Tserkovnyak, Antiferromagnetic spintronics, Rev. Mod. Phys. **90**, 015005 (2018).

[45] T. Jungwirth, X. Marti, P. Wadley, and J. Wunderlich, Antiferromagnetic spintronics, Nat. Nanotechnol. **11**, 231 (2016).

[46] P. Němec, M. Fiebig, T. Kampfrath, and A. V. Kimel, Antiferromagnetic opto-spintronics, Nat. Phys. **14**, 229 (2018).

[47] E. V. Gomonay and V. M. Loktev, Spintronics of antiferromagnetic systems, Low Temp. Phys. **40**, 17 (2014).

[48] S. Toyoda, M. Fiebig, T.-h. Arima, Y. Tokura, and N. Ogawa, Nonreciprocal second harmonic generation in a magnetoelectric material, Sci. Adv. **7**, eabe2793 (2021).